Received 1 October 2024; revised 1 November 2024; accepted 22 November 2024. Date of publication 29 November 2024;
date of current version 13 December 2024.

Digital Object Identifier 10.1109/OJCOMS.2024.3508717

Body Area Network Channel Measurement and Modeling for Extended-Reality Applications

CARLOS H. ALDANA[1] (Senior Member, IEEE), KOICHIRO TAKAMIZAWA[2], SHRUTHI SOORA[2], CONNOR KENNEDY[1], MORTEZA MEHRNOUSH[1,3], JAMEELIA COOK-RAMIREZ[2], CHUNYU HU[1,4], AND ANDREAS F. MOLISCH[5] (Fellow, IEEE)

[1]Reality Labs, Meta Platforms, Menlo Park, CA 94025, USA
[2]WRC Technologies Group, Wireless Research Center North Carolina, Wake Forest, NC 27587, USA
[3] Apple Inc, CA, USA [4]Spreadtrum Communications, San Diego, Los Altos CA 92121, USA
[5]USC Viterbi School of Engineering, University of Southern California, Los Angeles, CA 90089, USA

CORRESPONDING AUTHOR: C. H. ALDANA (e-mail: caldana@meta.com)

The work of Andreas F. Molisch was supported by the Meta Platforms.
Part of this work was presented at the IEEE International Conference on Communications 2022 [37] [DOI: 10.1109/ICC45855.2022.9838426].

ABSTRACT Extended reality (XR) headsets often need to communicate with devices mounted on the body, which could be sensors or computation devices, creating a body area network (BAN). To design reliable communication systems for these purposes, an accurate model for the propagation channel in such a head-centric BAN needs to be established. This paper presents a set of measurements of ultrawideband (UWB) channels of such a BAN when the user is in an indoor office environment. Based on this, we derive a novel model for link gain as a function of the location of the device on the body. This model distinguishes the power received via (i) on-body propagation, (ii) reflections from close-by objects, and (iii) reflections from other parts of the environment. For the on-body and near-by object reflections, we further introduce a new model for the link gain that depends on both the Euclidean distance and the azimuthal positions of the RX antenna elements on the circumference of the body. The measurements and derived models are first motivated by measurements on an RF phantom. Measurements on four human users covering all combinations of male/female and low/high body mass index are then used to parameterize this model.

INDEX TERMS Body area networks, virtual reality, path loss, delay dispersion, channel model, channel propagation.

I. INTRODUCTION

A. MOTIVATION

OVER the past decade, interest in Virtual Reality (VR) and Augmented Reality (AR), often together called Extended Reality (XR), has constantly increased. XR has the potential to revolutionize the work environment: for example, XR is used for professional training for dangerous situations without the need of actually subjecting the trainees to physical danger; for conveying instructions to workers on the field as they are working on a particular object; for having better interaction in teleconferences than can be achieved with traditional video conferencing. At the same time, XR promises to open new forms of information and entertainment to consumers: for example, XR guides for tourists can identify buildings and overlay historical information, and XR games can be more immersive and interactive than those played on computer monitors.

The headset is the centerpiece of an XR setup; however, in most circumstances, it needs peripherals that are mounted on the body. Firstly, many applications require sensors on the body that need to communicate with the headset. Secondly, for applications requiring significant processing, the computing unit is difficult to integrate into the headset and is a separate device, often mounted on the body or carried in a backpack for improved mobility. Wireless connectivity is the preferred method for communication between the headset and peripheral units, as it eliminates the potential for cable entanglement and associated safety risks.

In order to achieve high data rates and obtain precise localization information from the sensors (which is required

for many XR applications), the connections should have a large bandwidth. For this reason, ultra-wideband (UWB) communications are envisioned for XR applications using the IEEE 802.15.4ab standard, which enhances the IEEE 802.15.4z standard [1], an extension of the 802.15.4a standard [2]. UWB is allowed in the U.S. for the frequency range $3.1 - 10.6$ GHz, but due to interference from other systems, it is effectively restricted to frequencies larger than 6 GHz. Furthermore, the official deployment rules in several countries limit the emissions to frequencies larger than 6 GHz.

Like for any wireless system, the design and assessment of such UWB-based XR-Body Area Networks (BANs) requires knowledge of the propagation channel in which the system will operate. The purpose of this work is to get an indication of what the link propagation conditions would look like in normal cases and extreme cases: normal weight individuals (according to the American Heart Association) ($18.5 < \text{BMI} < 24.9$) and severely obese individuals (BMI >40) [3], [4]. Note that the existence of UWB standards does not imply that system design and evaluation are finalized; the standard only describes the implementation of transmitters (TXs) but not receivers (RXs), and furthermore, the standard does not make prediction of the system's performance quality. Thus, the existence of a standard does not obviate the need for channel models for the propagation channel in typical XR settings. A model based on the approach of this paper is currently being considered by the IEEE 802.15 group for use in future refinements of the standard.

B. EXISTING WORK

BAN propagation channels have been investigated for several decades. Measurements have mainly been done for narrowband applications, in particular in the ISM bands. The use of the 2.45 GHz band is often motivated by BANs based on the Bluetooth standard, while the 400 and 900 MHz band are often motivated by medical applications. Measurements have been performed in anechoic chambers, as well as indoor and outdoor environments, using human test subjects and RF phantoms; we refer to the literature surveys in [5], [6]. Obviously, all of these results cannot be applied to UWB systems near 8 GHz, both due to the different center frequency and the smaller bandwidth of the measurements.

Detailed investigations into UWB BAN channels have also been conducted. In particular, the 802.15.4a channel model [7] contains a model for UWB channels in an anechoic environment based on EM simulations. The 802.15.6ma model [8] contains a revision of the original 802.15.6 model and covers both human and vehicle body area networks. With regard to measurements from head to body, no new measurements or simulations have been added. Measurement-based models have been based on measurements both inside an anechoic chamber and a lab or office environment, using a phantom [9], a single person [10], [11], [12], [14], [15], [16], [17], [18], [24], or groups of people [6], [13], [19], [20], [21], [22], [23]. The impact of the antenna type on such measurements is discussed in [24]. The impact of the location of the hub (in head, torso, etc.) on the performance of the system in narrow bands within the 5-7 GHz range was analyzed in [25]. These models cover mostly the entire frequency range $3.1 - 10.6$ GHz and usually describe both path loss and delay dispersion. However, links are mostly between different parts of the torso, or between limbs and torso, and are thus different from the head-centric links required for XR-BANs.

The number of UWB experimental investigations in which at least one of the nodes is on the head is rather limited. Several papers investigate the propagation around the head, i.e., TX and RX on different sides of the head [9], and [26], [27] (which are narrowband). Reference [28] measured from a single point on the arm to several points on the body so that body-to-head links are included, but there are only four measured links; the measured environment is an office. Similarly, [16], [18], [19], [20], [22], [23], [24], [29], [30] measured from a single point on the torso to various locations on the body, performing measurements in an anechoic chamber, giving multiple measured links. Reference [31] expanded on the work done in [30] and used electromagnetic simulations to predict path loss and focused on BMI and waist circumference as a way to predict path loss for five simulated subjects in the $3.1-4.8$ GHz band. Reference [32] measured the propagation in the $1 - 12$ GHz range, from the head to several points on the body (arms, torso, legs) in both an anechoic chamber and a conference room; [33], [34] provides more extensive descriptions of those measurements, including detailed investigations on sources of variability and the impact of antenna spacing from the body. The former paper describes (among other extracted quantities) the link gain as a function of distance; however, the use of a traditional power law (as a function of Euclidean distance) leads to very high standard deviations (on the order of 15 dB); the latter paper also discusses separability of on-body and environment-reflected signal components. Reference [35] measures head to body links, but in a completely different frequency range (94 GHz). The work in [36] focused on the propagation characteristics of the ear-to-ear at 2.4 GHz. Different types of body-worn antennas for head-centric communications were considered and a channel model based on creeping waves along the head was derived.

The closest work to our goals is [22], which performed and analyzed extensive BAN measurements between more than 100 different locations on the body that included multiple positions on the head. However, the model that is extracted from those measurements aims for a statistical description of the fading with the ensemble of the different measurement locations, mixing results between head-based and non-head-based links. Thus, this analysis does not provide a dependence of path loss on the specific placement of the nodes on the body, which is the aim of the present paper. A similar constraint holds for [19], which differs further from our goals by taking measurements in a different frequency

range of $3-5$ GHz, [25] which takes measurements in the range of $5-7$ GHz, and [20] which takes measurements in the range of $3-10$ GHz.

On-body propagation is of course strongly impacted by the body shape. However, this effect is rarely considered in existing papers: most of the UWB BAN measurements in the literature are based on a phantom, or a single person. Exceptions to this are [19], which analyzed the difference between propagation characteristics of three people with different weights in the frequency range of 3−5 GHz in an anechoic chamber; [20], which measured $3-10$ GHz channels on eight different male test subjects with various body types in a lab environment, where the transmitter (TX) was on the hip, and the receiver (RX) nodes distributed over the front of torso and legs; and [6], which measured 60 male test subjects with various body mass indices in the $3-10$ GHz range, again with TX or RX on the hip. None of these measurements included a device on the head. One possible reason for the limited number of channel models from head to body involving humans is the extreme measurement effort and the required Institutional Review Board (IRB) approval at universities to make measurements involving humans.

C. CONTRIBUTION OF WORK

As the above literature survey has shown, there currently is no placement-dependent UWB model for propagation channels between head and torso that accounts for different body types of the wearers and the considered environment. The purpose of this paper is to fill this gap. In particular,

- We present extensive head-centric UWB ($4.5-8.5$ GHz) BAN measurements on four different test subjects, covering the combinations of male/female and low/high body mass index. Further measurements on an RF phantom are also provided.
- We introduce a novel model structure for BANs that distinguishes on-body, near-object reflections, and far-away environments, and can thus more flexibly combine precision measurements on the body with information about environmental reflections in a variety of environments.
- We model the link gain[1] due to on-body and near-object reflections with a new approach that depends not only on the Euclidean distance between TX and RX but also takes the relative circumferential angle (or angle offset) on the body into account. Simple closed-form fitting equations are provided.
- We present the parameterization of the model for the different test subjects.

The results can thus be used as the basis for designing and assessing UWB BAN systems for XR applications. Although the principles of the model and parameterization were described in our conference paper [37], that paper did not provide details of the measurement campaigns, parameterized only based on the phantom, which does not consider the effect of different body mass indices, and used only a 500 MHz bandwidth.

D. ORGANIZATION OF REMAINDER OF PAPER

The remainder of this paper is organized as follows: Section II describes the measurement setup, environment, and details of the campaign. Section III presents the signal processing method as well as sample results for the measured impulse responses. Next, the link gain model is motivated, derived, and parameterized. A summary concludes this paper.

II. MEASUREMENT CAMPAIGN

This section describes the measurement setup, the test subjects and the environments in which the measurements were made.

A. MEASUREMENT SETUP

The measurements were done in the frequency domain, with a vector network analyzer (VNA), specifically the SC5090 model of Copper Mountain Technologies. This approach was chosen because of the high accuracy of (calibrated) measurements that can be achieved with such a setup. The measured frequency range was chosen as $4.5-8.5$ GHz. This was partly related to the characteristics of the chosen antenna (see below) and partly out of the necessity to keep the measurement duration reasonably low. For some test measurements, the frequency step width was chosen as 1 MHz, corresponding to a measurable excess delay of multipath components (MPCs) of 300 m. Those measurements verified that a spacing of 5 MHz is actually sufficient, leading to an (un-aliased) excess delay of 200 ns $=$ 60 m. The intermediate frequency (IF) of the VNA was set to 3 kHz for most measurements. Additional measurements were taken with a smaller IF bandwidth (1 kHz), which further improved the signal-to-noise ratio (SNR) but which turned out to be superfluous.

The TX port was connected via an RF switch (using HP RF Switch Control Model 3488A) to two antennas mounted on the left and right sides of the head (see below), and the RX port to four antennas. The cables leading from the switch to the antennas were SMA cables from Mini-Circuits CBL-10FT-SMSM+ and CBL-12FT-SMS+, specified up to 18 GHz and 4 m long; the cables leading to the antennas on the body were 3.3 m long. VNA, switch, and cables leading to the antennas were calibrated with an electronic calibration kit (Copper Mountain model ACM2520), with the calibration reference plane at the SMA connector at the antennas.

All measurements were repeated ten times directly, one after each other, for human subjects; for phantom measurements, 20 repetitions were used. This served for two purposes: (i) it enables noise averaging, if required, and

[1]Since we measure here the combination of antennas and channel, we use the expression "link gain" for the ratio of RX power divided by TX power. The "path gain" is traditionally defined as the contribution of the propagation channel alone, with the antenna effects excluded.

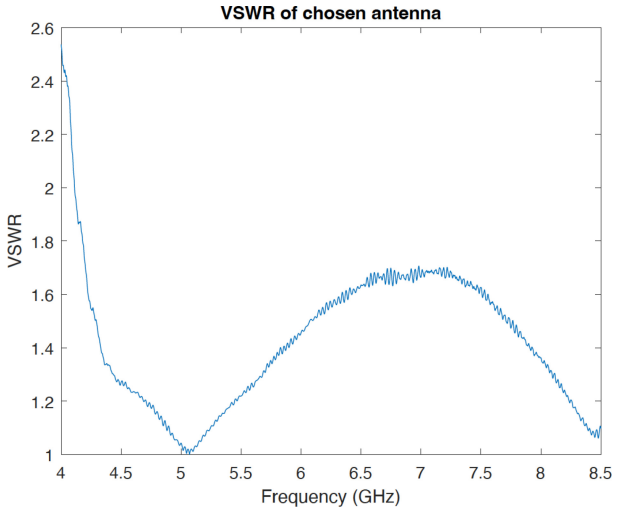

FIGURE 1. VSWR of measurement antenna.

(ii) in particular in the case of measurements on the human subject, it allowed to track the variations in the received power due to residual movement - while the test subjects were requested to stay still during a measurement sweep, movement from breathing and other small involuntary movements are unavoidable.

The antennas used were AVX / Electrotronics Model 1005194 UWB antennas [38], which are linearly polarized and compact (dimensions 20.6 x 18.6 x 0.8 mm). The antenna is optimized to have 6.1 dBi peak gain for $6-8.5$ GHz, but the actual samples used had acceptable VSWR (Voltage Standing Wave Ratio) (<2) from $4.1-9$ GHz, see Fig. 1. For our applications, not only is the frequency dependence of the VSWR important, but the antenna pattern plays an important role because the antenna responses are interpreted as a component of the radio channel that we characterize. The derived conclusions are antenna dependent. Fig. 2 shows the antenna pattern at 4.5, 6.5, and 8.5 GHz. These characteristics were measured in a 3D spherical antenna test chamber. The antenna pattern measured in free-space can be seen in Fig. 2 to be reasonably omni-directional. The contour plots are representation of the 3D antenna pattern in a 2D format and can be viewed in a fashion similar to that of a spherical globe to a 2D world map. The top and bottom of the contour plot are equivalent to the poles, and the center is equivalent to the equator. During measurements, a separation distance from the body of at least 9mm was shown to provide consistent return loss greater than 10 dB between various antenna samples. To maintain this separation distance, a foam spacer measuring 4mm thick was added between the antenna and 5mm thick Velcro. Future work may consider smaller separation distances from the body.

The two TX antennas were placed pointing towards the floor, on the left and right side of a mock-up of XR glasses, thus being placed near the left and right temple. The antenna arrangement was not mirror-symmetric: since the radiating

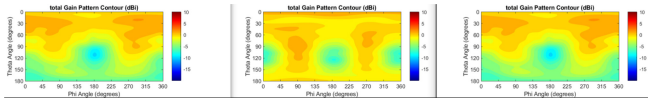

FIGURE 2. Antenna pattern at 4.5 (left), 6.5 (middle), and 8.5 (right) GHz in free space.

sides of each patch antenna must be oriented away from the head, and the antenna connectors (and their associated cable arrangements) both need to be above the antennas for mechanical stability, the antennas are placed such that a nominal "zero degree" is oriented towards the front of the head on the left side, and towards the back of the head on the other side. This is important because it implies that even under ideal circumstances we cannot expect mirror-symmetric arrangements of the RX antennas on the body to result in mirror-symmetric channel impulse responses.

The antenna characteristics mentioned above were measured for the antenna in free space. However, large dielectric objects distort the pattern. We first measured the impact of the head on the radiation characteristics, as shown in Fig. 3; the head of a modular whole-body phantom, referred to as Popeye (POsable Phantom for Electromagnetic sYstems Evaluations), was detached from the torso and placed in the anechoic chamber; the results are shown in Fig. 5. Since the whole phantom itself was too large to be placed in the test chamber, the effect of the torso was emulated by placing the antenna on a bottle filled with dielectric liquid with properties similar to the phantom, as shown in Fig. 4. The distorted antenna pattern is shown in Fig. 6. The deviations from an isotropic pattern are more pronounced than in the free-space case. This leads to a higher sensitivity to the specifics of the placement on the human body, the directions of dominant radiation, and the relative orientation of the TX and RX antennas.

B. TEST SUBJECTS AND ANTENNA MOUNTS

Measurements were first performed on an RF phantom called Popeye. This is a brand of phantoms manufactured by SPEAG AG [39] and certified for over-the-air testing, emulating the average dielectric and loss properties of the human body. The phantom used for most of the measurements was the SPEAG Popeye version 5.5. The specific model used in the measurement campaign emulates the body type of a male in good physical shape (used by the Canadian army). The phantom was used both because of the availability for repeated experiments and because of the inherent time-invariance of its shape. The RX antennas were placed pointing towards the headset on different locations of the torso, using velcro strips to allow easy detachment and reproducible re-attachment; alignment markers indicated the exact location on the torso. To maintain constant spacing between the phantom and antenna, thick foam spacers were used so that the back of the antenna was 9 mm from the body, including the width of the velcro. Our investigations with different spacings confirmed the results of [33] on the

FIGURE 3. Antenna mounted on phantom head.

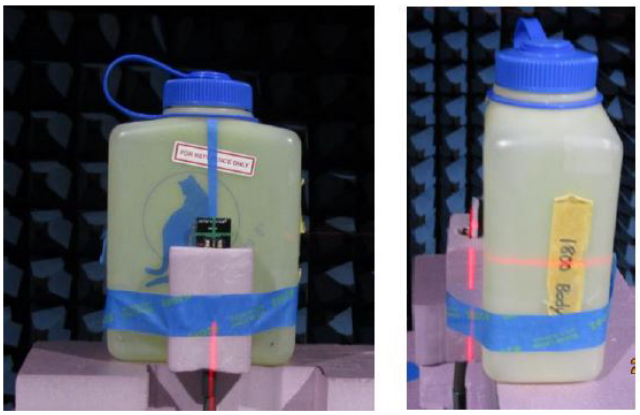

FIGURE 4. Antenna mounted on bottle filled with phantom fluid.

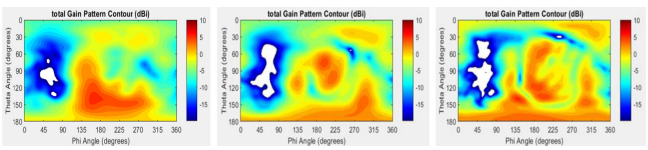

FIGURE 5. Antenna pattern at 4.5 (left), 6.5 (middle), and 8.5 (right) GHz for mounting on phantom head.

importance of spacing in antenna characteristics and link gain.

Since stability of the phantom when standing is a problem, only the head, arms, and torso were used, and placed on a stack of styrofoam bricks that were placed on a plastic cart, so as to minimize reflections from the mounting, see Fig. 7.

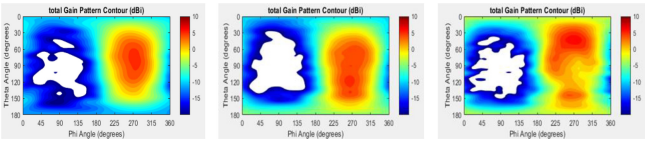

FIGURE 6. Antenna pattern at 4.5 (left), 6.5 (middle), and 8.5 (right) GHz for mounting on bottle filled with phantom fluid.

FIGURE 7. Photo of human phantom "Popeye" in the "Office with Desk" environment.

FIGURE 8. Photo of human phantom "Popeye" with antennas and cabling.

Antennas were placed on the phantom on a vertical line on the left side of the torso (directly under the TX antenna on the left side of the head), with a distance from that TX antenna of 30, 40, 50, and 60 cm. Furthermore, the antennas were placed on the circumference of the body, at angles $n \times 30°$, $n = 0, 1, 2, \ldots, 11$, at a vertical distance of 50 cm from the TX. The cables for both TX and RX antennas were carefully placed and fixed in place to minimize the impact on antenna patterns and propagation paths from TXs to RXs, see Fig. 8.

The remainder of the measurements were performed on human test subjects. For each subject, a set of measurements were made in 10 vertical and 12 circumferential positions, respectively. Measurements were recorded for the left and right TX antennas on the head. Although the mounting of the TX antennas was the same, the mounting of the RX antennas was different, since the gluing of velcro strips on the body was not an option. Rather, we constructed a harness that could be placed on the test subjects, with the velcro strips located on the harness, see Fig. 9. Each test subject

(a) Subject A

(b) Subject B

(c) Subject C

(d) Subject D

FIGURE 9. Photos of the four measurement subjects.

had a custom made harness specifically designed to fit their body. The harness was made with velcro straps that ran over the tops of the shoulders down the front and back of the body, down to the ankles. To secure the harness to the body of the test subject, velcro was wrapped around the body at the ankles, thighs, and waist. There were nylon buckle straps velcroed to the chest and upper back to keep the harness on the shoulders. Due to height variations between test subjects, body parts were used as a reference to keep the location of the 10 vertical positions at similar points on the body. The armpit and just below the kneecap were used as starting and stopping heights for the vertical antenna body positions. The other 8 vertical body antenna positions were placed along the front left side of the body, an equal distance between the arm pit and upper shin. On each test subject, these positions were at different heights depending on the test subject's body. The location of the antennas of the RX antennas relative to the TX antennas was determined separately for each of the test subjects with a laser localization arrangement; for the fits of the link gain to the distance, the thus-determined Euclidean distance is used.

The circumference around the waist was taken in the vertical 50 cm position of each test subject and recorded. 12 antenna positions on the harness were marked an equal distance apart. The first antenna at $\phi = 0°$ was placed in the front center of the test subjects. The other antennas were placed around the waist at every 30° up until $\phi = 330°$.

Several structures were used to support the weight of the cables and keep them in place with respect to the test subjects. Velcro wrap was added to the head RF cables to keep them secured to the side of the goggles (headset mockup) and to help hold the antenna in place. The test subject wore a non-metallic cap with velcro straps to secure the RF cables connected to the head antennas. Behind the test subject was an RF-transparent foam support fixture. This fixture was used to keep the weight of the RF cable from pulling the antennas off the goggles. The foam support fixture also helps to keep the cables from running too close down the back of the person, possibly interfering with some body antenna positions and test configurations. The VNA was placed approximately 1m to the side of the test subjects and was also covered with RF-absorbent material. The absence of significant echoes from the thus-covered VNA was verified in the anechoic chamber.

The four test subjects were recruited via a dedicated ad campaign and selected to provide all combinations of male / female and normal / high body mass index (BMI). Full information about the tests was provided and written consent was obtained from all test subjects according to standard ethical procedures. In this paper, test subjects are labeled in order of their measurement campaigns as subject A-D. Photos of the test subject are shown in Fig. 9, with faces made unrecognizable for privacy reasons.

- *Subject A* is male, with a height of 178 cm and weight of 70 kg, leading to a BMI of 22. The custom harness was created for this test subject with the V30 cm position 30 cm below his eyeline and the V120 cm position 120 cm below his eyeline. The V50cm position was at 50 cm below the eyeline. At this height, the body circumference was 89.5 cm.
- *Subject B* is female, with a height of 189 cm and a weight of approximately 180 kg, which leads to a BMI of 51. The custom harness was created for this test subject with the V30 cm position being 25.5 cm below her eyeline and V120 cm position being 130 cm below her eyeline. The V50 cm position was 48.7 cm below the eyeline. At this height, the body circumference was 149 cm.

- *Subject C* is male, with a height of 179 cm and a weight of 171 kg, resulting in a BMI of 53. The custom harness had the V30 cm position at 39.5 cm below his eyeline and V120 position 133.5 cm below his eyeline. The circumference positions at the V50 cm height were 54 cm below the eyeline. The test subject's circumference around the torso height was 146.3 cm.
- *Subject D* is female, with a height of 157.5 cm and a weight of 53 kg, resulting in a BMI of 21. The harness made for her had the V30 cm position at her arm pits, 26 cm below her eyeline. The V120 position landing in the upper part of the shin at 116 cm below the eyeline. The circumference positions at the V50 cm height were 46 cm below the eyeline. The test subject's circumference around the torso at this height was 84 cm.

It is well recognized that BMI is not the only factor determining body shape; see also the discussion in [6]. We stress that we use the terms "high BMI" and "normal BMI" as convenient shorthand for the body types of the test subjects. The propagation conditions in a person with a high BMI due to athletic build, with weight created mainly by muscle mass, will be different than, for example, in Subject C.

C. ENVIRONMENT

The measurements with the phantom were performed in three environments: (i) an anechoic chamber, (ii) an empty office, where the phantom was placed in the center of the office, and (iii) an office with furniture, including a standing desk and monitor, with the phantom placed in front of the desk. The office had dimensions 3.5 × 3.9 m; in the office with the desk, the phantom was in front of the desk, with a distance of approximately 1.25 m from the wall behind the desk.

Measurements with human test subjects were made in an office environment only. The setup was similar, though for Subject D, the standup desk was adjusted downward so that the top of the monitors was in line with test subject's eyeline. For Subject C, the subject's feet were placed so that his feet were 137 cm from the wall behind the desk; this was done to have sufficient spacing between the belly of the subject and the edge of the desk.

III. DATA PROCESSING AND SAMPLE RESULTS

A. DATA PROCESSING

This paper only considers the link gain between TX and RX; to model delay dispersion with 500 MHz bandwidth, we refer to our conference paper [37]; delay dispersion with full bandwidth for both phantoms and humans will be considered in our future work. For the evaluation of link gain, the antennas are considered as part of the propagation channel, since a de-embedding of the antenna characteristics is very difficult, particularly when placing antennas on different parts of the body. Thus, as mentioned above, we consider the link gain, not the channel gain. The output of the measurements is a 5-dimensional matrix $H_{i,j,k,m,e}$, where i and j index the position of the RX and TX antennas, respectively, k is the frequency bin $k = 0, \ldots, 800$, m indexes the repetition of the measurement $m = 0, \ldots, 9$ (or $m = 0, \ldots, 19$, since 20 repetitions were made for the measurements on Popeye). The parameter e denotes the environment (for the case of the phantom) or the test subject (for human measurements).

The first processing step is the (coherent) averaging over the 10 (or 20) measurement repetitions. We then obtain for each combination i, j an 801 element vector that is extended with nulls in the frequency domain to 4096 entries. This representation is then multiplied with two different frequency-domain filters: (i) a rectangular filter with bandwidth 4 GHz (i.e., an identity operation), and (ii) a Kaiser filter with parameter $\beta = 3.2$, resulting in a 3 dB bandwidth of approximately 2 GHz. In each case, the resulting signal then undergoes an inverse fast Fourier transform (IFFT), providing an oversampled version of the impulse response $h(\tau)$, and the power delay profile $P(\tau) = |h(t, \tau)|^2$ with a sample spacing of approximately 50 ps. The different frequency-domain filters are used for different purposes: the results from the rectangular filtering are used for the computations of the powers, since only this version provides equal weighting for the different frequency components over the considered bandwidth. The impulse responses based on the Kaiser filter serve to visualize the impulse responses and find the separation between the different "zones" of the impulse response, as outlined below; the absence of significant sidelobes is important for these tasks.[2] In either case, the impulse responses are then delay gated, such that all MPCs with delay larger than 120 ns (equivalent to 36 m range) are disregarded, to avoid "wraparound" contributions from a strong initial component to contribute to the environmental MPCs Note also that the impulse response contains the group delay of the TX/RX antenna pair, which is approximately 350 ps. Since we interpret the antennas to be part of the channel, we do not correct for that group delay but keep in mind that the measured delays of, e.g., a line-of-sight (LOS) peak are therefore shifted compared to where they would be expected from purely geometrical considerations.

One of the key steps in our modeling (see Section IV) will be the distinction between MPCs that propagate on the body, those that propagate via nearby objects such as the desk, computer screen, and possibly the floor, and those propagating via farther away environmental objects including the room walls (except for the wall directly behind the desk, which is counted as "nearby object"). The distinction between those walls can be made via delay filtering. For establishing the delay thresholds between the zones, we used a combination of geometric consideration and visual inspection of the power delay profiles. In particular, we

[2]The Kaiser-filtered impulse response will also serve in future work for modeling of delay dispersion, whose accuracy would suffer significantly from the sidelobes of the sinc function resulting from the rectangular filtering.

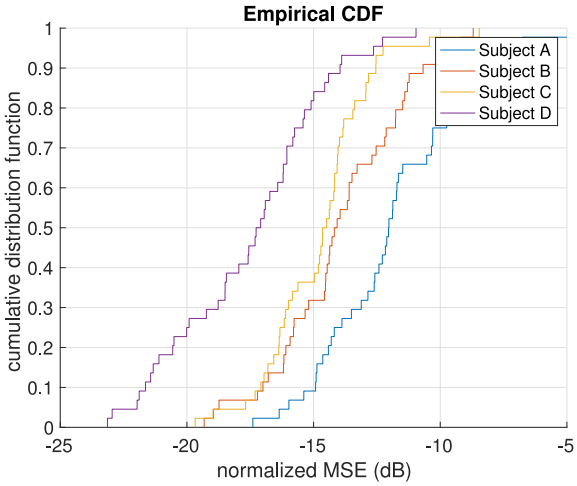

FIGURE 10. Cdf of the received power standard deviation due to breathing.

choose the threshold θ as

$$\theta = \tau_{\mathrm{Gr}} + \tau_{\mathrm{LOS}} + 0.75(\tau_{\mathrm{ReflN}} - \tau_{\mathrm{LOS}}) \tag{1}$$

where τ_{Gr} is the antenna-pair group delay, τ_{LOS} is the delay corresponding to the geometrical (LOS) distance between TX and RX, and τ_{ReflN} is the delay corresponding to the reflected component. The asymmetric placement of the threshold between the LOS and the reflected component is motivated by the fact that delayed (compared to LOS) components propagating on the body are possible, while precursors of the reflected component are only due to sidelobes. Visual inspection of all measured power delay profiles (PDPs) confirmed the above choice.

B. POTENTIAL ERROR SOURCES

As for any measurement, there are potential sources for errors and inaccuracies. We list in the following their origin and our measures to counter and/or quantify them.

- *Calibration errors in the VNA*: VNAs are only accurate when properly calibrated with a calibration kit. Calibration was performed daily. After all measurements, all the cables, antennas, and adaptors were cleaned and covered with dust caps.
- *Movement of the subjects during the measurements:* The duration of each measurement run (10 repetitions of the VNA scans was 7-10 s). During this time the test subjects were breathing in and out, leading to variations of the channel. In order to assess the possible magnitude of this, we analyzed the power variations between the different recordings of the same measurements. We compute the standard deviation for each measurement location, and in Fig. 10 plot the cdf of the variations over the different RX locations on the body, showing a separate cdf for each of the four test subjects. We can see that in almost all cases, the normalized mean square error is less than -10 dB. We also find that Subject A moved the most, while subject D moved the least. Since both these subjects were low-BMI, there is no indication that the BMI plays a role in the amount of residual movement. Similarly, female subject B had more motion than male subject C, but male subject A has much more motion than female Subject D. Again, there is thus no indication of an impact on the amount of motion.
- *Change of the posture and antenna mounting during the measurement campaign:* The measurements of one test subjects lasted over more than one day, so that at several occasions the harness had to be taken off and placed on the test subjects again. While effort was made to move the harness back to the same position, it was not possible to guarantee this. Furthermore, the test subjects sat down to rest and got up again between measurement sets, and it could not be guaranteed that they took on exactly the same posture (their location in the room was reproducible since the location for the feet was marked). In order to assess the possible impact of these changes, we analyzed measurements done with one test subject (Subject A) at 31 occasions.[3] Fig. 11 shows the cumulative distribution function of the deviation from the received mean powers over the ensemble of occasions. We see that the variations are small for the RX antenna mounted at 30 cm vertical distance from the TX; from this we can infer that either the head position was not changed significantly, or small movements of the head have a small impact on the RX power. However, for 50 cm distance, both on the front and the back of the body, the variations are considerably larger, and can reach 10 dB in extreme cases. We conjecture that the posture of the body plays a major role, since it impacts both the orientation of the RX antenna with respect to the TX antenna, and the abundance of tissue shadowing off the link.
  We also note that different clothes or slight changes in body type over the duration of the measurement campaign could, in principle, create variations of the results. However, since the measurements were performed on subsequent days and the test subjects were asked to wear the same clothes, these error sources were not considered to be applicable.
- *Imperfect separation of the different MPC zones:* The separation of the MPCs into different zones, as described above, is imperfect due to the delay dispersion of the antenna pairs, and the fact that no clear "empty zone" exists between the on-body and reflected components. A quantification of this effect is attempted for the case of Popeye, by comparing the received power in the anechoic chamber by the delay-filtered on-body contribution in the empty office, and the desk scenario.

[3]Measurements were taken at 31 different locations in a large hall for a location of the RX at 50 cm vertical and $\phi = 0°$ and $\phi = 180°$); delay filtering as described above was used to extract the on-body component only.

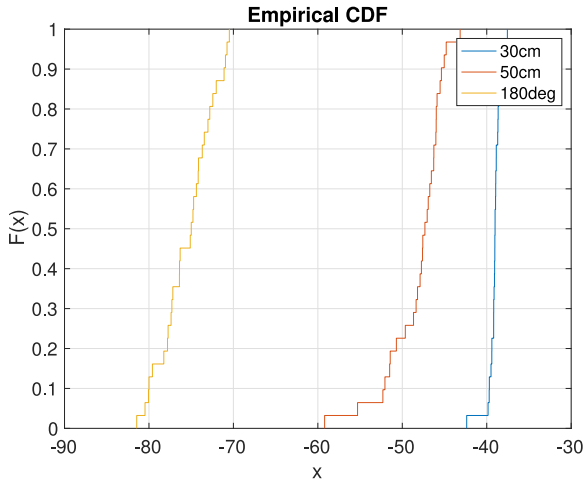

FIGURE 11. Cdf of the received power standard deviation due to change in posture of Subject A at 31 different occasions. Results for RX location at 50 cm vertical distance and $\phi = 0°$ and $\phi = 180°$.

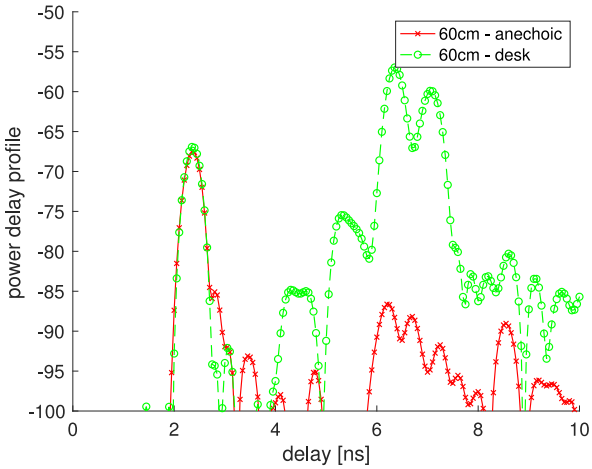

FIGURE 12. Power delay profile [in dB] (Kaiser filtered) for TX on the left side of the head, and RX 60 cm below the TX. Note that the "on-body" zone ends at 3.9 ns according to the geometrical considerations used in this paper to divide the zones.

Fig. 12 shows the comparison for the location 60 cm below the eye level; while there are some differences in the shape of the main lobe, those differences carry only small energy.[4] However, it is possible that the error is larger for RX locations on the legs, since there the run length difference between on-body and desk-reflected components is larger; yet this case could not be measured due to the absence of legs on our phantom.

- *"Spillover" of sidelobes:* Since for the computation of the power we use rectangular frequency domain windows that give rise to *sinc* sidelobes in the delay domain, some of the sidelobes of MPCs located in one zone "spill over" to other zones. A judicious choice of the zone boundaries helps minimize this error. The spillover from the on-body zone into the "near objects" zone is furthermore mitigated by the fact that for the case that the on-body contribution is very strong (i.e., transmission to the front of the body, with short distance between TX and RX) the delay of this contribution is far from the zone boundary.

[4]Other sample comparisons of PDPs in the chamber and the desk environment showed somewhat larger differences, including differences in the peak magnitude; from physical considerations it seems likely that this stems from different placement angle of the antennas, since no environmental MPCs can impact the main peak.

C. SAMPLE RESULTS

Fig. 13 shows several sample results of the PDP in an office environment with a desk (for clarity, only the delay range $[0, \ldots, 25ns]$ is shown), using the Kaiser-filtered version of the PDP to avoid sidelobes. These figures overlay the responses for Subjects A-D, allowing to see the impact of the body shape of the test subjects. In Fig. 13a, the TX is directly above the RX, only 30 cm away. In the region up to about 5 ns, we see a pronounced peak corresponding to the direct connection between TX and RX; note that it is not possible to distinguish from the measurements whether a free-space LOS connection is associated with this peak, or a surface wave (or a combination thereof). A second strong peak can be seen around 7 ns, corresponding to the screen reflections. The environmental reflections, which start around 12 ns only shown up to a delay of 25 ns, since otherwise details of the earlier reflections would not be well visible. We note that the differences between the PDPs of the different subjects are minor.

Fig. 13b shows the PDP when the RX is 50 cm below the TX antenna. We observe that the screen-reflected components have remained essentially unchanged, while the direct component has decreased by more than 6 dB, that is, more than the 4.4 dB expected from Friis' law. Furthermore, the variations between users are significantly higher than for the case of 30 cm distance. The RX antenna is mounted on the belly, which for some of the subjects is shadowed off by the chest, while for others, the RX is located on a protruding belly.

Fig. 13c shows the PDP when the RX is on the center of the back side, 50 cm below the TX antenna. We observe that the direct component is severely attenuated for all subjects.

Fig. 13d shows the PDP when the RX is 110 cm below the TX antenna. We observe that the direct component is non-existent for subjects B and C and is still present for subjects A and D. Here we see that the body shape plays a significant role in the direct component.

If the RX is on the back of the phantom, the direct component (diffracting around the body and / or propagating as a surface wave) is strongly attenuated, as can be seen in Fig. 13c. Furthermore, the screen-reflected MPC is almost completely absent. Rather, MPCs propagating via back and sidewall reflections provide the dominant contributions. Again, this applies to all the test subjects, but the details of the relative strengths differ.

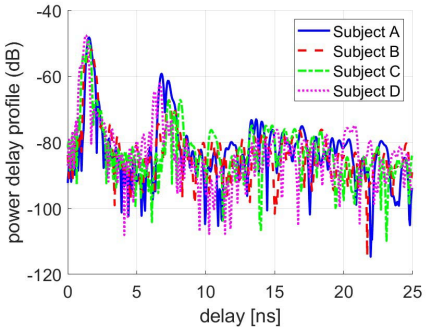

(a) Left head to left side of body 30 cm below.

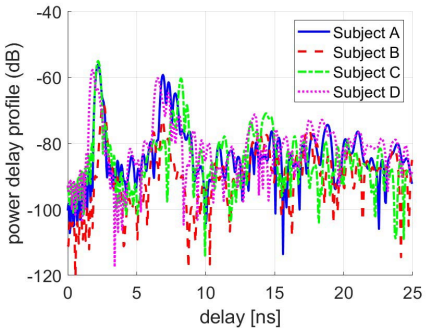

(b) Left head to left side of body 50 cm below

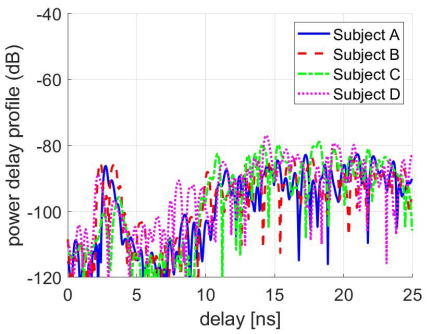

(c) Left head to spine (center of back) 50 cm below

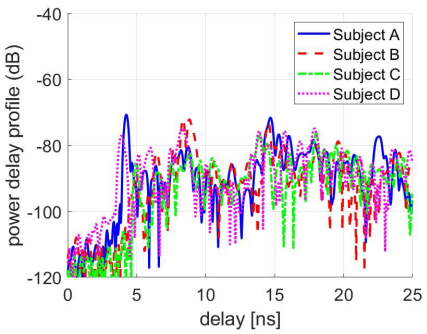

(d) Left head to left side of body 110 cm below

FIGURE 13. Squared magnitude of impulse response for channel from head to body in office environment with desk, for the four human subjects.

IV. MODEL

To model the channel in the considered environments, we propose splitting the MPCs into contributions of on-body propagation, reflections from nearby objects (if they occur), and room reverberations. One key advantage of this approach is that the on-body propagation, which is always present, but most difficult to model, can be measured once, e.g., in an anechoic chamber (or a room in which separation of the on-body component can be done through delay filtering). It can then later be combined with the room reverberations from a variety of environments, such as office, residential, industrial hall, etc. To validate this idea, we compared the on-body contributions of Popeye in chamber and desk environment, as shown in Fig. 12.

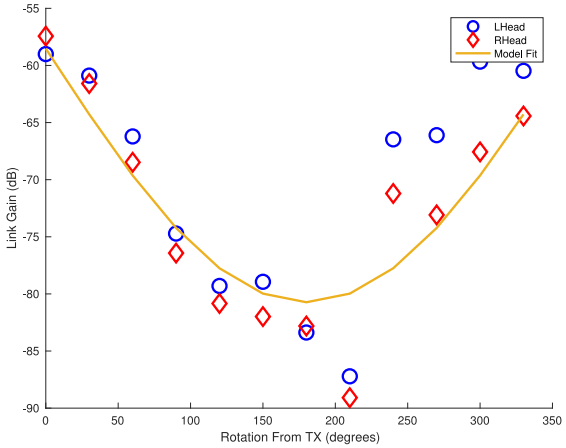

FIGURE 14. Link gain from the left and right side of the head to the different positions on the circumference on the body, and sinusoidal fit.

Furthermore, the link gain in each zone can be described by a combination of a term dependent on the Euclidean distance between TX and RX (mostly determined by the vertical distance) and a term depending on the angle of the RX on the body. In the following, we first show the basic structure of the model as obtained from measurements with the phantom, and subsequently describe the measurements with the human test subjects.

A. LINK GAIN MODEL FOR ON-BODY PROPAGATION

We first analyze the dependence of the link gain on the position of the RX antenna along the circumference of the body. Since the Euclidean distances between the TX and the different RXs are almost identical, a traditional power-distance model would describe the gain as essentially constant. A slightly more advanced model, which distinguishes between LOS and NLOS would have a discontinuity when transitioning from the position with LOS and NLOS and also raises the difficulty on how to define LOS and NLOS.

We propose here a new empirical fit based on inspection of our measurement results. Fig. 14 shows the link gain on the phantom for both situations when the TX antenna is on the left and right side of the head. In the coordinate system of the measurements, $\phi = 0°$ is defined to be vertically below the TX (at around $\phi' = 30°$ for the left TX in the absolute coordinate system that has its origin on the sternum,

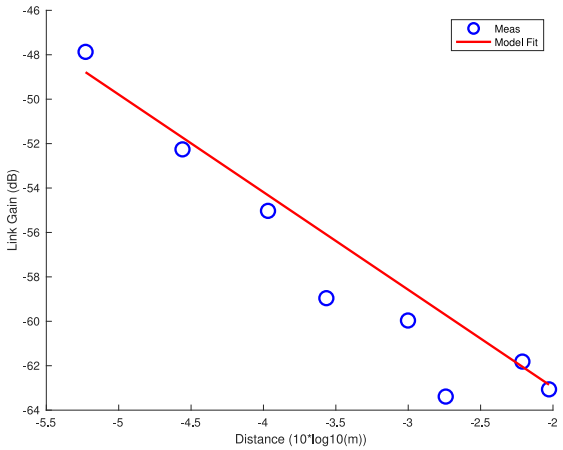

FIGURE 15. Link gain from the left side and right side (adjusted for circumference displacement) of the Popeye head to the different positions on the front of the body, and linear fit.

and $\phi' = 330°$ for the right TX). The angle increases with counter-clockwise rotation for the left TX, and clockwise for the right TX, thus creating better symmetry between the two considered situations.[5] A good fit for the dependence of the link gain on the angle is a sinusoidal dip (the negative half of a sinewave)

$$G_{\mathrm{c,dB}}(\phi) = \alpha_{\mathrm{c}} + \beta_{\mathrm{c}} \sin(\phi/2) + S_{\mathrm{c}} \tag{2}$$

where ϕ is the *difference in angle* between the location of the TX and the observation point, S_{c} are shadowing variations with standard deviation σ_{c}, and α_{c}, β_{c}, and σ_{c} are parameters to be extracted from the measurements.

Note that this model assumes that *only* the angle difference is relevant, which would be logical if the body were rotationally invariant, i.e., a (circular) cylinder. Since human bodies are more elliptical in shape, one may expect that, e.g., two TX locations that are on the front of the body would have a smaller link gain difference than, e.g., one point on the front and one of the back, even if the angular difference is the same for the two cases. Yet, in the interest of simplicity and to keep the number of free parameters low (and thus avoid overfitting), we use the above model. The impact of this simplification will be discussed below.

For the dependence of the link gain on the vertical distance, we use the traditional power law

$$G_{\mathrm{v,dB}}(d) = \alpha_{\mathrm{v}} + 10\beta_{\mathrm{v}} \log(d/d_0) + S_{\mathrm{v}} \tag{3}$$

where d_0 is the reference distance that we arbitrarily set to 1m, and the other parameters have an interpretation similar to that for the circumference model. Note that d here denotes the Euclidean distance between TX and RX (which, under most circumstances, is very close to the purely vertical distance). The circumferential loss is thus the *excess* loss compared to the Euclidean loss at the $\phi' = 30°$ location.

[5]Note that this is different from our conference version [37], which always used counter-clockwise coordinate systems.

TABLE 1. Fitting parameters for on-body contribution of the link gain.

Subject	A	B	C	D	phantom
β_{v}	-3.48	-6.56	-7.63	-4.94	-4.39
α_{v}	-60.1	-74.4	-70.8	-65.3	-71.8
β_{c}	-28.0	-20.9	-32.8	-30.0	-22.2
σ_{V}	3.76	5.1	5.08	3.86	1.80
σ_{C}	6.89	6.8	7.14	7.40	4.82

TABLE 2. Fitting parameters for near-object contribution of the link gain.

Subject	A	B	C	D	phantom
β_{v}	-2.92	-1.23	-3.01	-2.08	-0.94
α_{v}	-64.6	-62.2	-67.4	-62.4	-56.0
β_{c}	-27.9	-22.9	-24.1	-26.1	-28.8
σ_{V}	3.40	4.27	2.57	2.85	1.52
σ_{C}	4.58	4.44	5.16	4.3	3.00

TABLE 3. Fitting parameters for environment contribution of the link gain.

Subject	A	B	C	D	Phantom
β_{v}	-0.41	-0.20	-0.05	-0.42	-0.79
α_{v}	-64.5	-62.9	-62.7	-61.9	-65.1
σ_{V}	1.96	1.67	2.64	1.7	1.83
σ_{C}	2.07	2.14	2.76	2.62	2.36

Since the circumference measurements were done at a vertical distance of 0.5m, a consistent model will then ensure that $\alpha_{\mathrm{c}} = \alpha_{\mathrm{v}} + 10\beta_{\mathrm{v}} \log(0.5)$. In other words, link gain can be obtained, for any location and angular offset as,

$$G_{\mathrm{c,dB}}(\phi) = \alpha_{\mathrm{v}} + 10\beta_{\mathrm{v}} \log(d/d_0) + \beta_{\mathrm{c}} \sin(\phi/2) + S. \tag{4}$$

The parameters of this model are summarized in Tables 1–3. We first find a large intercept value α_{v}, which is caused by the fact that our chosen reference distance is *larger* than the distances at which we measure (this, of course, has no impact on the results). We secondly observe a strong dependence of the link gain on the distance, with a slope of more than 6, compared to a free-space slope of 2. This strong distance dependence is partly caused by the fact that at farther distances, intervening body parts shadow off the free-space connections. Another contribution might arise from the fact that the antenna is placed tangential to the body shape at the mounting location, so that different RX locations have the RX antenna with different angles with respect to the vertical line and thus different antenna gains.

In Figure 16 we have a comparison of the proposed phantom channel model in the case when $\phi = 0°$ (front) and $\phi = 180°$ (back) with the 802.15 WBAN models in [18], [40]. We see results similar to those of the work in [40], where measurements are made along the body ($\phi = 0°$) and around the body ($\phi > 0$), with the transmitter in the torso region. We also see that our $\phi = 0°$ model is similar to the one in [18], which had all TX and RX antennas placed in front of the body.

Note 1. The measurements are asymmetric in that the RX locations are directly below the left TX, but offset by some

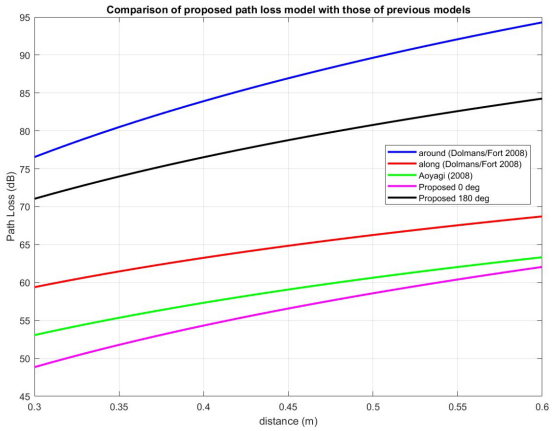

FIGURE 16. Comparison with 802.15 BAN channel models. Note that this plot shows link loss = negative gain.

60° for the right TX. Consequently, the measured link loss for the right TX needs to be adjusted (boosted in power) when fitting the vertical link loss model. In our conference paper [37], we used an adjustment of $\beta_c \sin(60°/2) = \beta_c/2$, which is consistent with the circumferential model. However, inspection of the results for not only Popeye, but also the four human subjects, showed that this leads to an overcompensation related to the fact that both RX positions are on the front of the body, and thus the difference in their link gains should be smaller than $\sin(60°/2) = 1/2$, as discussed above. Here, we use an *empirical* adjustment factor of $\beta_c/4$; this reduces the standard deviation of the measurement results from the fit by about 1 dB.

Note 2. At this time, it is only a conjecture that the link gain indeed follows this model; in particular it is possible (and even likely) that β_c depends on the vertical distance d. However, since no measurements are available that would allow one to verify this hypothesis and quantify such a dependence, we retain the simple model (4). It is important to keep in mind that measurements with human subjects are inherently time-limited and measurements that encompass all combinations of distances and angles are very time consuming. Such time consumption is mainly governed by the time needed to move the RX antennas to the different locations on the body, so that using, e.g., a time-domain setup instead of a VNA would not significantly reduce the measurement time.

B. LINK GAIN FOR NEAR-OBJECT REFLECTIONS

The basic principle of fitting the contribution from near-reflected objects is similar to the on-body case. Using the principle of image sources, one can visualize the MPCs are LOS components emanating from behind the computer screen or stand-up desk (depending on the actual reflection point). The points on the front of the body will thus receive significantly more energy than those on the back. However, in contrast to the on-body model (and different from our conference paper [37]), the exact position of the RX of the body does not matter *as long as this location is on the front of the body*. This is due to the fact that the virtual sources are at a distance of more than 2 m, and thus all just have pure LOS with almost identical Euclidean distance (for the same reason, the offset between left and right TX becomes irrelevant). For RXs *on the back of the body*, it is now the absolute azimuth angle ϕ' that is relevant, not the angle difference ϕ, because the diffraction around the body is determined by the relative position of the body to the screen/desk and thus the virtual sources. The circumferential link gain is thus written as,

$$G_{\mathrm{c,dB}}(\phi') = \begin{cases} \alpha_\mathrm{c} + \beta_\mathrm{c} \sin(\phi' - \pi/2) + S_\mathrm{c} \\ \text{for } \pi/2 \le \phi' \le 3\pi/2 \\ \alpha_\mathrm{c} + S_\mathrm{c} \quad \text{otherwise.} \end{cases} \tag{5}$$

The vertical dependence and the interaction between vertical and circumferential fit are modeled in the same way as for the on-body propagation.

C. LINK GAIN FOR ENVIRONMENTAL CONTRIBUTIONS

The "environmental" contributions (more precisely, long-delayed MPCs that are reflected by the far walls in the office, and/or multiple reflections) show very little dependence of the link gain on the circumferential position of the body. When fitting with the same type of model as for near-reflections, we obtained β_c on the order of $1-2$dB, i.e., much smaller than the standard deviation of the fluctuations. This is in line with intuition: in the extreme case of a reverberation chamber, where the MPCs are reflected many times with attenuation, the angular spectrum of the radiation at the RX is flat. For this reason, we inherently set $\beta_\mathrm{c} = 0$. Note that depending on the particularities of the room, non-flat angular spectra might occur, but the location of a potential dip in the spectrum might not be at the back of the human, and might be in a direction that depends on the environmental properties only (e.g., an open window from which there are no reflections); it might be desirable to make appropriate ad hoc modifications of the model on a case-by-case basis.

The vertical dependence is also rather weak, and one could arguably set the slope of the link loss curve to zero (in particular, since the 95% confidence intervals encompass both positive and negative slopes). However, the geometry of the setup suggests that when the reflection coefficient of the floor is significantly different from that of the walls, a distance dependence might occur; we thus leave the dependence in.

D. LINK GAINS FOR THE DIFFERENT SUBJECTS

We now turn to the link gain results for the different subjects. Note, again, that the fits for Popeye are based on circumferential measurements and vertical measurements from 30 to 60 cm distance, while the human subjects contain the circumferential measurements and vertical measurements from 30 to 120 cm.

Fig. 17 shows the vertical dependence of the on-body link gain for the four different human subjects. We observe here a significant difference between low-BMI and high-BMI

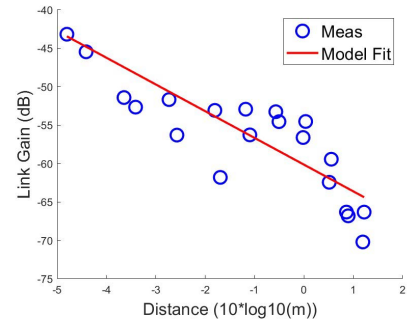

(a) Subject A

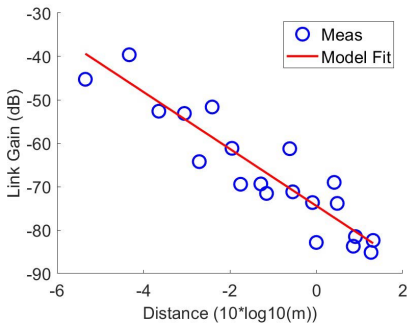

(b) Subject B

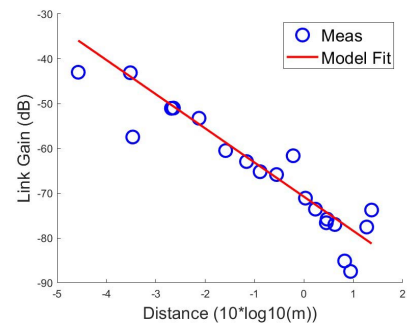

(c) Subject C

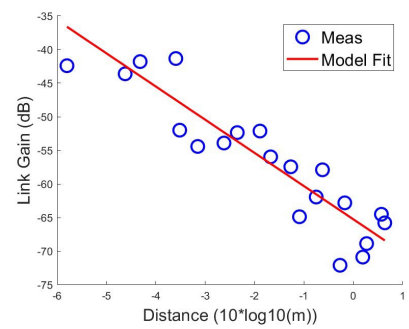

(d) Subject D

FIGURE 17. Link gain for human subjects as function of Euclidean distance for vertical points.

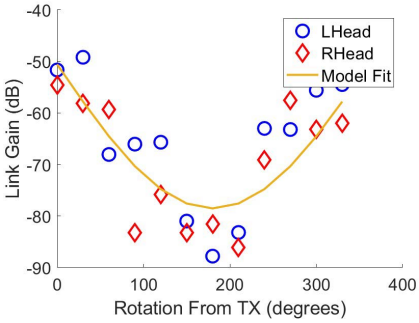

(a) Subject A

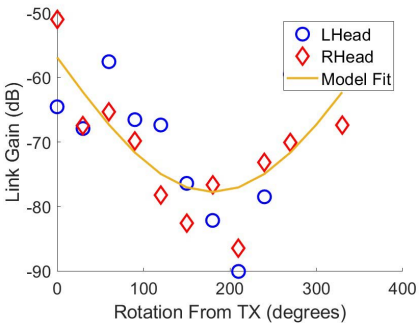

(b) Subject B

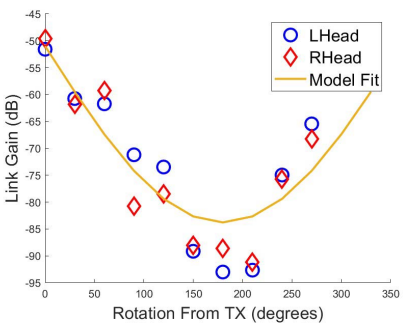

(c) Subject C

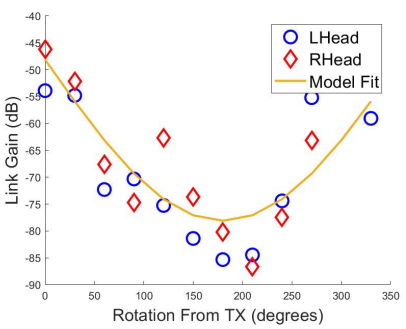

(d) Subject D

FIGURE 18. Link gain for on-body propagation for human subjects as a function of offset angle.

subjects: the minimum link gain in the former case (subjects A and D) is around -70 dB, while for subjects B and C it approaches -90 dB. The maximum link gain in all cases is around -40 dB, which is intuitive since the propagation to a location on the front of the body near armpit height does not depend much on the body type.

Fig. 18 shows the dependence of the link gain on the circumference angle offset ϕ. We see that the agreement

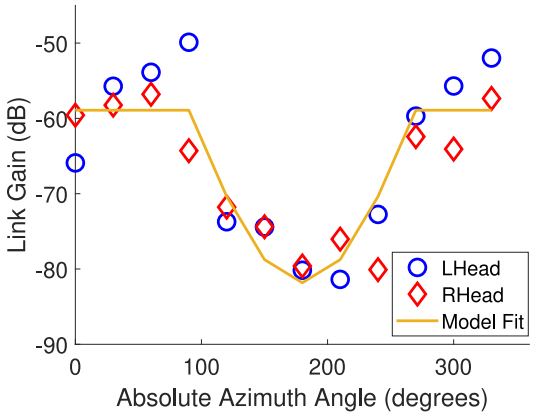

(a) Near-object reflected contributions

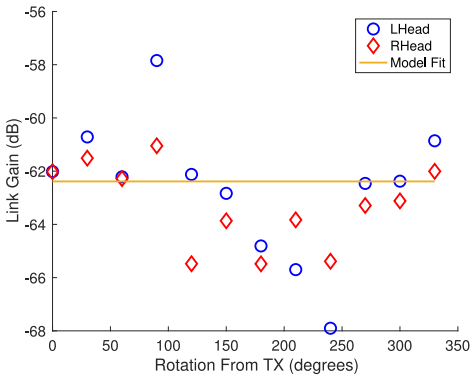

(b) Environmental (circumferential)

FIGURE 19. Link gain of near-object reflected contributions and environmental reflections for human test subject B.

of the measured values with the model shape (sinusoidal) is reasonable - it is visually better in some cases (e.g., Subject D) than in others (Subject A), though the computed standard deviations are all on the order of 7 dB. The "worst-case" attenuation is actually on the order of 40 dB (while β_c is around -30 dB).

To demonstrate the effect of the near-object reflections, Fig. 19a shows the circumferential dependence of the screen-reflected power in subject B. We see that the model fits the data reasonably well.

The contributions from the environment are shown for Subject B in Fig. 19b. The results confirm that a modeling of the angular dependence is not necessary, as discussed above.

Tables 1-3 summarize the extracted parameters for all human test subjects, as well as the phantom.

V. CONCLUSION

This paper introduced a new model, based on extensive measurements, for the link gain in UWB BANs ($4.5 - 8.5$ GHz) where one end of the link is mounted on the head and the other on the torso or legs. Such models are important for the design and optimization of wireless systems used in XR devices. In particular, we performed the measurements with an RF phantom, as well as four different test subjects that covered all combinations of male/female and high/low BMI. From the measurement results, we motivated and parameterized a novel model for the radio channel.

Firstly, we divide the contributions to the received power into (i) on-body propagation, (ii) reflections from nearby objects, and (iii) reflections from far objects in the environment. In general, the link loss equation becomes $10^{\frac{onbody}{10}} + 10^{\frac{screen}{10}} 1_{scenario} + 10^{\frac{env}{10}} 1_{scenario}$, where $1_{scenario}$ is an indicator function of the scenario and determines whether there is a screen and / or walls present. The various contributions were extracted through delay filtering, and the division of the received power into those three contributions justified by three arguments: (i) they arise from different physical propagation mechanisms, (ii) they show different dependencies on distances and angle differences between TX and RX, and (iii) it is possible to obtain results for different combinations of people and environments with a significantly reduced measurement effort - for example, changing the dimensions of the room, and thus strength of the environmental contributions is mostly independent of the body shape of the human subjects and their on-body propagation. Finally, the pure on-body component is the only one guaranteed to be present in any type of environment (e.g., outdoor), and can thus be interpreted as a worst-case scenario from an SNR point of view. However, long-delayed components of the environment might strain a limited-complexity equalizer.

We also introduced a novel model for on-body propagation that depends not only on the Euclidean distance but also on the angular difference between TX and RX. We showed that this model provides a more accurate characterization of the effects of placing the RX at various points on the back of the user. A similar model also explains the angular dependency of the link gain from near-object reflections.

Future work will focus on modeling the delay dispersion of the channel. Preliminary investigations in [37] showed that for 500 MHz bandwidth, the on-body and near-object reflection can be represented by a single delay tap each, but by going to higher bandwidths, a much more complicated PDP arises also for these contributions.

ACKNOWLEDGMENT

The authors would like to thank Carl Murray for fruitful discussions in IEEE 802.15.4ab.

REFERENCES

[1] P. Sedlacek, M. Slanina, and P. Masek, "An overview of the IEEE 802.15.4z standard its comparison and to the existing UWB standards," in *Proc. 29th Int. Conf. Radioelektronika (RADIOELEKTRONIKA)*, 2019, pp. 1–6.

[2] J. Zhang, P. V. Orlik, Z. Sahinoglu, A. F. Molisch, and P. Kinney, "UWB systems for wireless sensor networks," *Proc. IEEE*, vol. 97, no. 2, pp. 313–331, Feb. 2009.

[3] "Overweight & obesity statistics." Accessed: May 26, 2023. [Online]. Available: https://www.niddk.nih.gov/health-information/health-statistics/overweight-obesity

[4] C. D. Fryar, M. D. Carroll, and J. Afful. "Prevalence of overweight, obesity, and severe obesity among adults aged 20 and over: United States, 1960-1962 through 2017-2018." NCHS Health E-Stats. 2020. [Online]. Available: https://www.cdc.gov/nchs/data/hestat/obesity-adult-17-18/obesity-adult.htm

[5] D. B. Smith, D. Miniutti, T. A. Lamahewa, and L. W. Hanlen, "Propagation models for body-area networks: A survey and new outlook," *IEEE Antennas Propag. Mag.*, vol. 55, no. 5, pp. 97–117, Oct. 2013.

[6] S. Sangodoyin and A. F. Molisch, "Impact of body mass index on ultrawideband MIMO BAN channels—Measurements and statistical model," *IEEE Trans. Wireless Commun.*, vol. 17, no. 9, pp. 6067–6081, Sep. 2018.

[7] A. F. Molisch et al., "A comprehensive standardized model for ultrawideband propagation channels," *IEEE Trans. Antennas Propag.*, vol. 54, no. 11, pp. 3151–3166, Nov. 2006.

[8] T. Kobayashi, D. Anzai, M. Hernandez, M. Kim, and R. Kohno, "Channel modeling activities of international standardization on IEEE 802.15 TG6ma for human and vehicle body area networks," in *Proc. IEEE 17th Int. Symp. Med. Inf. Commun. Technol. (ISMICT)*, 2023, pp. 1–6.

[9] T. Zasowski, G. Meyer, F. Althaus, and A. Wittneben, "UWB signal propagation at the human head," *IEEE Trans. Microw. Theory Tech.*, vol. 54, no. 4, pp. 1836–1845, Jun. 2006.

[10] A. Fort, J. Ryckaert, C. Desset, P. De Doncker, P. Wambacq, and L. Van Biesen, "Ultra-wideband channel model for communication around the human body," *IEEE J. Sel. Areas Commun.*, vol. 24, no. 4, pp. 927–933, Apr. 2006.

[11] A. Fort, C. Desset, P. De Doncker, P. Wambacq, and L. Van Biesen, "An ultra-wideband body area propagation channel model-from statistics to implementation," *IEEE Trans. Microw. Theory Tech.*, vol. 54, no. 4, pp. 1820–1826, Jun. 2006.

[12] A. Fort, F. Keshmiri, G. R. Crusats, C. Craeye, and C. Oestges, "A body area propagation model derived from fundamental principles: Analytical analysis and comparison with measurements," *IEEE Trans. Antennas Propag.*, vol. 58, no. 2, pp. 503–514, Feb. 2010.

[13] T. Kobayashi, "Recent progress of ultra wideband radio propagation studies for body area network," in *Proc. 2nd Int. Symp. Appl. Sci. Biomed. Commun. Technol.*, 2009, pp. 1–6.

[14] T. Zasowski, F. Althaus, M. Stager, A. Wittneben, and G. Troster, "UWB for noninvasive wireless body area networks: Channel measurements and results," in *Proc. IEEE Conf. Ultra Wideband Syst. Technol.*, 2003, pp. 285–289.

[15] J. Teo, S. W. Chan, Y. Chen, E. Gunawan, K. S. Low, and C. B. Soh, "Time domain measurements for UWB on-body radio propagation," in *Proc. IEEE Antennas Propagat. Soc. Int. Symp.*, 2007, pp. 325–328.

[16] Q. H. Abbasi, M. U. Rehman, S. Liaqat, and A. Alomainy, "Multiple input multiple output radio channel characterisation for ultra wideband body centric wireless communication," in *Proc. IEEE Int. RF Microw. Conf. (RFM)*, 2013, pp. 238–242.

[17] H. Ghannoum, C. Roblin, and X. Begaud, "Investigation and modeling of the UWB on-body propagation channel," *Wireless Pers. Commun.*, vol. 52, no. 1, pp. 17–28, 2010.

[18] T. Aoyagi et al., "Channel model for wearable and implantable WBANs," IEEE, Piscataway, NJ, USA, document 802.15-08-0416-04-0006, 2008.

[19] X. Chen, X. Lu, D. Jin, L. Su, and L. Zeng, "Channel modeling of UWB-based wireless body area networks," in *Proc. IEEE Int. Conf. Commun. (ICC)*, 2011, pp. 1–5.

[20] M. M. Khan, M. A. Rahman, A. Alomainy, and C. Parini, "Ultra wideband on-body radio radio propagation channels study for different real human test subjects with various sizes and shapes," in *Proc. 2nd Int. Conf. Adv. Elect. Eng. (ICAEE)*, 2013, pp. 323–328.

[21] F. Di Franco et al., "The effect of body shape and gender on wireless body area network on-body channels," in *Proc. IEEE Middle East Conf. Antennas Propagat. (MECAP)*, 2010, pp. 1–3.

[22] R. Di Bari, Q. H. Abbasi, A. Alomainy, and Y. Hao, "An advanced UWB channel model for body-centric wireless networks," *Prog. Electromagn. Res.*, vol. 136, pp. 79–99, Jan. 2013.

[23] Q. Wang, T. Tayamachi, I. Kimura, and J. Wang, "An on-body channel model for UWB body area communications for various postures," *IEEE Trans. Antennas Propag.*, vol. 57, no. 4, pp. 991–998, Apr. 2009.

[24] A. Sani et al., "Experimental characterization of UWB on-body radio channel in indoor environment considering different antennas," *IEEE Trans. Antennas Propag.*, vol. 58, no. 1, pp. 238–241, Apr. 2009.

[25] V. Sipal, D. Gaetano, P. McEvoy, and M. J. Ammann, "Impact of hub location on the performance of wireless body area networks for fitness applications," *IEEE Antennas Wireless Propag. Lett.*, vol. 14, pp. 1522–1525, 2014.

[26] D. Bresnahan and Y. Li, "Investigation of creeping wave propagation around the human head at ISM frequencies," *IEEE Antennas Wireless Propag. Lett.*, vol. 16, pp. 2767–2770, 2017.

[27] R. Chandra and A. J. Johansson, "A link loss model for the on-body propagation channel for binaural hearing aids," *IEEE Trans. Antennas Propag.*, vol. 61, no. 12, pp. 6180–6190, Dec. 2013.

[28] L. Xia, S. Redfield, and P. Chiang, "Experimental characterization of a UWB channel for body area networks," *J. Wireless Commun. Netw.*, vol. 2011, Jan. 2011, Art. no. 703239. [Online]. Available: https://doi.org/10.1155/2011/703239

[29] T. Kumpuniemi, T. Tuovinen, M. Hämäläinen, K. Y. Yazdandoost, R. Vuohtoniemi, and J. Iinatti, "Measurement-based on-body path loss modelling for UWB WBAN communications," in *Proc. 7th Int. Symp. Med. Inf. Commun. Technol. (ISMICT)*, 2013, pp. 233–237.

[30] B. Youssef and C. Roblin, "Statistical modeling of WBAN channels in indoor environments based on measurements and ray tracing," in *Proc. 15th Eur. Conf. Antennas Propagat. (EuCAP)*, 2021, pp. 1–5.

[31] B. Youssef and C. Roblin, "A statistical assessment of anthropomorphic characteristics impacts on WBAN communications," in *Proc. 16th Eur. Conf. Antennas Propagat. (EuCAP)*, 2022, pp. 1–5.

[32] L. Traver, C. Tarin, D. Toledano, C. Roblin, A. Sibille, and N. Cardona, "Head to body UWB-BAN channel measurements," *Eur. Cooper. Field Sci. Techn. Res.*, vol. 2100, pp. 18–19, May 2009.

[33] C. Roblin et al., "Antenna design and channel modeling in the BAN context part II: Channel," *Ann. Telecommun., Annales des téléCommun.*, vol. 66, no. 3, pp. 157–175, 2011.

[34] C. Roblin, "On the separability of 'on-body' and 'off-body' clusters in the modeling of UWB WBAN channels for various indoor scenarios," in *Proc. 5th Eur. Conf. Antennas Propag. (EUCAP)*, 2011, pp. 3148–3152.

[35] P. Usai, A. Monorchio, A. Brizzi, A. Pellegrini, L. Zhang, and Y. Hao, "Analysis of on-body propagation at W band by using ray tracing model and measurements," in *Proc. IEEE Int. Symp. Antennas Propag.*, 2012, pp. 1–2.

[36] K. Jakobsen, "Progress in body-worn antennas for on-body propagation," in *Proc. Int. Symp. Antennas Propagat. (ISAP)*, 2016, pp. 130–131.

[37] C. Aldana, C. Kennedy, M. Mehrnoush, C. Hu, and A. F. Molisch, "Body area network channel model for virtual-reality applications," in *Proc. IEEE Int. Conf. Commun.*, 2022, pp. 2519–2524.

[38] "AVX Ethertronics UWB PCB antenna with SMA connector," Data Sheet, AVX Corp., Fountain Inn, SC, USA. Accessed: Aug. 2, 2024. [Online]. Available: https://datasheets.kyocera-avx.com/ethertronics/AVX-E_1005194.pdf

[39] "SPEAG Swiss." Accessed: Aug. 2, 2024. [Online]. Available: http://speag.swiss

[40] G. Dolmans and A. Fort, "Channel models WBAN—Holst centre/IMEC-NL," IEEE, Piscataway, NJ, USA, document 802.15-08-0418-01-0006, 2008.